International Journal of Greenhouse Gas Control 87 (2019) 66–79

Contents lists available at ScienceDirect

International Journal of Greenhouse Gas Control

journal homepage: www.elsevier.com/locate/ijggc

CO_2 plume migration and dissolution in layered reservoirs

Gege Wen[a,*], Sally M. Benson[b]

[a] Department of Energy Resource Engineering, Stanford University, Stanford, Rm 153, 367 Panama St, Stanford, CA 94305 USA
[b] Department of Energy Resource Engineering, Stanford University, Stanford, Suite 324, Rm 315, 473 Via Ortega, Stanford, CA 94305 USA

ARTICLE INFO

Keywords:
CO_2 storage
Heterogeneity
Plume footprint
Dissolution

ABSTRACT

In carbon capture and storage (CCS) projects, the presence of layered permeability heterogeneity can strongly affect the migration of the supercritical CO_2 plume and CO_2 dissolution. By conducting a systematic study of plume migration in layered reservoirs with a wide range of permeability contrast between the layers, we show that the relationship between CO_2 plume footprint and permeability contrast has three distinct regimes. For moderate permeability contrasts from 1 to 5, the presence of different layers has little impact on plume migration. As the contrast increases from 5 to 50, the plume footprint decreases progressively. In the event of extreme contrast (> 50), the footprint is smallest and independent of the heterogeneity. Overall, the footprint of the plume can vary by more than 2-fold, with large implications for monitoring, access to sites, and regulatory issues. The mass fraction of CO_2 dissolution can vary up to 2-fold depending on the degree of heterogeneity. We also show that the common practice of using permeability anisotropy to simulate multiphase flows in layered reservoirs works quite well in terms of plume footprint for permeability anisotropy ratios of up to 25, but large errors occur at more extreme contrasts.

1. Introduction

Carbon capture and storage (CCS) is a greenhouse gas mitigation strategy requiring injection of supercritical carbon dioxide (CO_2) into deep sedimentary formations for long term storage. Numerical simulation is the primary tool for predicting the fate and transport of CO_2 in the subsurface, designing injection operations, and used together with monitoring data to refine and calibrate geological models. In the United States, numerical simulation is required by EPA as part of the permitting process to determine the Area of Review (AoR) that delineates the region of pressure buildup caused by CO_2 injection activity (EPA, 2013). Another parameter, the footprint of the plume, defined as the maximum lateral extent of separate phase CO_2, is used throughout the regulatory process of planning, operating, monitoring, and stabilization of the plume footprint is key to the site closure decision. During site screening, estimation of CO_2 plume footprint is essential for identifying pore space ownership issues and potential acquisition of storage leases (Frailey, 2013). In risk assessment, the simulated plume footprint is used to help identify potential well infrastructures, faults, or fractures in the area that may provide leakage pathways (NETL, 2017). Consequently, the ability to model plume migration accurately is a prerequisite for implementing CO_2 storage projects.

At a minimum, simulation models for predicting plume migration solve spatially and temporally discretized mass and energy balance equations for multiphase flow of CO_2 and brine. Plume migration is controlled by the interplay of viscous, buoyancy, and capillary forces. Supercritical CO_2 typically has a density of 0.5 to 0.7 times that of water at storage reservoir temperatures and pressures. Consequently, buoyancy forces are large and play an important role in plume migration. Viscous forces are large near the injection well, but decrease linearly with radial distance away from the injection well. For lower permeability rocks, capillary entry pressures are typically high, creating locally important barriers or impediments to flow in heterogeneous reservoirs.

Sedimentary formations being used for storage often contain layered permeability heterogeneity that strongly affects the movement of injected CO_2 and the plume footprint (e.g. Cavanagh and Nazarian, 2014; Strandli and Benson, 2013; Doughty, 2010; Sung et al., 2014). Absent vertical heterogeneity, CO_2 will migrate buoyantly upwards until it encounters the reservoir seal and begins to flow laterally under the seal. Low permeability intra-reservoir shale layers baffle the vertical migration of CO_2 and typically result in larger plume volume and lower gas saturation (Hovorka et al., 2004). At the same time, dissolution trapping and residual trapping are enhanced since a higher volume of brine and rock interacts with free phase CO_2 (Doughty, 2010). Generally, permeability heterogeneity with longer correlation lengths

* Corresponding author.
E-mail address: gegewen@stanford.edu (G. Wen).

https://doi.org/10.1016/j.ijggc.2019.05.012
Received 11 January 2019; Received in revised form 9 May 2019; Accepted 11 May 2019
Available online 21 May 2019
1750-5836/

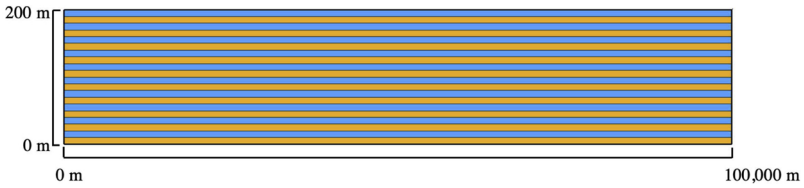

Fig. 1. Schematic of the heterogeneous reservoir. Blue represents higher permeability, brown represents lower permeability.

impose more influence on plume migration compared to heterogeneity with shorter correlation lengths (Ide et al., 2007). In reservoirs where permeability heterogeneity correlation length is short compared to the size of the plume (e.g. fluvial-type deposition), the plume footprints are broadened because (1) high shale content decreases total pore volume available for storage (Flett et al., 2007) (2) fluvial-typed heterogeneity architecture leads to a high degree of permeability anisotropy (Gershenzon et al., 2017). In the context of buoyancy-dominant systems with the "inject-low-and-let-rise storage strategy", the plume footprint is also broadened by short correlation length heterogeneity as CO_2 rises along preferential path of higher permeability (Bryant et al., 2006; Han et al., 2010). When the permeability heterogeneity correlation length is much shorter than flow length, the plume footprint may be unaffected by heterogeneity (Ide et al., 2007).

Grid orientation and resolution also have strong influences on predicted plume migration (Doughty and Pruess, 2004; Yamamoto and Doughty, 2011). Finite-difference grids tend to distort the plume in the grid orientation while radial grids can reduce this effect (Yamamoto and Doughty, 2011; Pruess and Nordbotten, 2011). Coarser grids generally underestimate plume footprint and overestimate average gas saturation due to suppressed gravity override and numerical dispersion (Doughty and Pruess, 2004). The degree of underestimation of the plume footprint is greater in heterogeneous models than for homogeneous models (Doughty and Pruess, 2004). In homogeneous models, a vertical grid on the order of a meter near the top of the reservoirs is considered effective in capturing the gravity override (Pruess and Nordbotten, 2011).

For reservoirs with layered continuous heterogeneity, it is a common practice to use the arithmetic average as the effective horizontal permeability and the harmonic average as the effective vertical permeability (Doughty and Pruess, 2004; Lengler et al., 2010; Strandli and Benson, 2013). In CCS models, anisotropic permeability is often employed when dealing with sections of highly heterogeneous reservoirs (Kumar et al., 2005; Lengler et al., 2010; Strandli and Benson, 2013; Zhang, 2013). However, the validity of using the permeability anisotropy in the context of CCS for predicting plume footprint and dissolution has not been established.

In addition to anisotropy in the absolute permeability, measurements in stratified heterogeneous cores show that the relative permeability curves are also an anisotropic property. A non-wetting phase often has a higher relative permeability when the flow direction is parallel to the bedding compared to when it is perpendicular. On the contrary, the wetting phase has a lower relative permeability in the direction that is parallel to the bedding (Corey and Rathjens, 1956; Iverson et al., 1996). Relative permeability can be anisotropic even for homogeneous and isotropic reservoirs due to gravitational forces (Prats and Lake, 2008). In the context of CCS simulations, the anisotropy of relative permeability should receive more attention because gravitational segregation and vertical displacement play an important role in CO_2 migration (Saeedi, 2012). However, the relative permeability is typically treated as an isotropic parameter in CCS models.

To address these issues, in this study, we systematically investigate the influence of purely layered and continuous intra-reservoir shales on plume footprint and CO_2 dissolution, including the effect of grid resolution. We also assess the degree to which and under what circumstances models using anisotropic permeability and relative permeability can be used to predict CO_2 plume migration and dissolution reliably.

2. Methodology

For these studies, we focus on thick reservoirs with layered heterogeneity such as the Mt. Simon Formation, in the U.S (Finley, 2014) and the Utsira Formation, offshore Norway (Zweigel et al., 2004). We use a purely layered system as an abstraction of the type of vertical heterogeneity observed in these formations to systematically investigate the relationship among layered heterogeneity, plume migration and CO_2 dissolution. We do not claim these are realistic models of any reservoir, but use them as a way to understand for the simplest of systems, how layered heterogeneities influence CO_2 transport. The model reservoir consists of 20 layers with alternating higher (sandy) and lower (shaley) permeability materials, where each layer is 10 m thick (Fig. 1). By decreasing the permeability and capillary entry pressure of shaley layers, we generate a series of synthetic reservoirs to investigate a range of increasing heterogeneity. The degree of heterogeneity is quantified by the "contrast ratio" defined as k_{high}/k_{low}.

A 2-D radial grid is used with progressively larger grid cells in the radial direction (Table 1). Grid cells have a uniform thickness of 0.5 m. The reservoir extends 100,000 m in the radial direction to simulate an infinitely acting reservoir. In Appendix A, we present a grid sensitivity study to justify the grid dimensions selected.

2.1. Model setup

2.1.1. Reservoir properties and injection parameters

The simulations are carried out in TOUGH2 using ECO2N (Pruess et al., 1999; Pruess, 2005). The system is simplified to be an isothermal water-CO_2 environment with reservoir temperature of 50 °C at a depth of 2000 m. The water table starts from 10 m below the ground surface and reservoir pressure is hydrostatic with reference to the water table. We assume a continuous CO_2 injection with a constant rate of 1000 metric tons/day (Q_{total}), injecting a total of 1 million tons over the 3-year period. The injection well is located in the center of this cylindrical reservoir and is perforated along the entire thickness of the reservoir. A simplified well model is used in which the fraction of the total injection allocated to each cell depends only on permeability as shown in Eqs. (1a) and (1b):

$$Q_{cell\ high\ k} = Q_{total} \times \frac{k_{high}}{k_{total}} = Q_{total} \times \frac{k_{high}}{10k_{high} + 10k_{low}} \quad (1a)$$

$$Q_{cell\ low\ k} = Q_{total} \times \frac{k_{low}}{k_{total}} = Q_{total} \times \frac{k_{low}}{10k_{high} + 10k_{low}} \quad (1b)$$

This approach neglects the fact that density differences between CO_2 and brine tend to increase the fraction of CO_2 injected into the upper portions of the formation. For the problem investigated here, these effects are small because the reservoir is relatively thin. In addition, this approach allows us to isolate the effects of permeability heterogeneity compared to other factors.

2.1.2. Material types

Properties of the rocks used for the simulations are listed in Table 2. We use Corey's Curve to model the relative permeability curves. Capillary pressure curves are constructed with the van Genuchten function. Fig. 2 shows the relative permeability curve used for all of the rocks and capillary pressure curves for a few representative materials.

Table 1
Description of the grid used for the systematic comparison of the influence of contrast ratio.

DIRECTION	NUMBER OF GRID CELLS	CELL SIZE (M)
Vertical	400	0.5
	Total thickness: 200 m	
Radial	2	0.17
	3	0.18
	5	1.8
	32	5.0
	53	10.0
	3	100.0
	5	1800.0
	5	18000.0
	Maximum radial extent: 100,000 m (closed boundary)	
Total number of grid cells: 43,200		

Table 2
Rock properties for simulation: permeability k in mD, permeability k in m^2, porosity ϕ, capillary entry pressure P_0 in Pa. P_0 is scaled by the Leverett J-function where k_{ref} = 3.95E-14 m2, ϕ_{ref} = 0.185 and P_{ref} = 7.5E3 Pa.

k (md)	k (m^2)	ϕ (-)	P_0 (Pa)
1000	9.87E-13	0.2	1.56E+03
500	4.93E-13	0.2	2.21E+03
400	3.95E-13	0.2	2.47E+03
250	2.47E-13	0.2	3.12E+03
200	1.97E-13	0.2	3.49E+03
100	9.87E-14	0.2	4.93E+03
80	7.90E-14	0.2	5.51E+03
50	4.93E-14	0.2	6.98E+03
40	3.95E-14	0.2	7.80E+03
20	1.97E-14	0.2	1.10E+04
10	9.87E-15	0.2	1.56E+04
8	7.90E-15	0.2	1.74E+04
5	4.93E-15	0.2	2.21E+04
4	3.95E-15	0.2	2.47E+04
2	1.97E-15	0.2	3.49E+04
1	9.87E-16	0.2	4.93E+04
0.8	7.90E-16	0.2	5.51E+04
0.5	4.93E-16	0.2	6.98E+04
0.4	3.95E-16	0.2	7.80E+04
0.2	1.97E-16	0.2	1.10E+05
0.1	9.87E-17	0.2	1.56E+05
0.08	7.90E-17	0.2	1.74E+05
0.05	4.93E-17	0.2	2.21E+05
0.04	3.95E-17	0.2	2.47E+05
0.02	1.97E-17	0.2	3.49E+05
0.01	9.87E-18	0.2	4.93E+05
0.008	7.90E-18	0.2	5.51E+05
0.004	3.95E-18	0.2	7.80E+05

3. Results

3.1. Supercritical CO_2 saturations and CO_2 dissolution

In the base case, the permeability of the sandy layers (k_{high}) is 500mD and the values of k_{high}/k_{low} range from 1 to 50,000. Fig. 3 shows results of the CO_2 saturations and the mass fraction of dissolved CO_2 for 7 representative reservoirs in the base case. A volume histogram of gas saturation for each model in the base case is shown in Fig. 4.

In homogeneous or weakly heterogeneous reservoirs ($k_{high}/k_{low} > 5$), supercritical CO_2 migration is governed primarily by buoyancy. The majority of the plume accumulates under the seal and migrates as a thin layer with high gas saturation (> 0.45). In this regime, the average saturations of the CO_2 plume are the highest among the base case models.

As the contrast ratio increases from 5 to 50, a progressively greater fraction of supercritical CO_2 remains deeper in the reservoir, trapped by the low permeability/high entry pressure layers. As a greater fraction of CO_2 is trapped deeper in the reservoir, the plume radius decreases progressively. In this regime, the bulk of the plume remains connected and the majority of the plume has low supercritical CO_2 saturation. The low gas saturation causes low relative permeability, which also contributes to the retention of CO_2 deeper in the reservoir. The second and third row of the histograms in Fig. 4 show bimodal distributions of CO_2 saturations, demonstrating that plumes with different saturations migrate in the different layers of the reservoir. Fig. 5 demonstrates that the saturation profiles in the reservoir are close to what is expected if they are in gravity capillary equilibrium.

When the contrast ratio further increases to greater than 50, the movement of CO_2 is hindered by the capillary barriers created by the shaley layers. In the case where the reservoir is extremely heterogeneous (e.g. k_{high}/k_{low} = 500mD/0.01mD), almost no CO_2 enters the lower permeability layers, and the plume can only travel in the high permeability layers. In this case, the plume in each layer is disconnected from those above and below it, except for the immediate proximity of the injection well. Again, the comparison of saturation profile in Fig. 5 shows that the separate plumes within each layer are in gravity-capillary equilibrium. We notice that the saturation distributions of the separate plumes are similar to the homogeneous reservoirs (Fig. 4). However, due to the relatively thin plumes in each layer, capillary pressures and consequently saturations are lower compared to more homogeneous cases. Lower saturation result in lower relative permeability, which also helps to reduce the influence of gravity override in the high permeability layers.

Summarizing the relationship between the plume radius and permeability contrast in Fig. 6, we recount that the rate by which the plume radius decreases can be divided into three regimes: permeability contrasts of 1 to 5, 5 to 50, and 50 and above. When the contrast ratio is between 1 and 5, the plume radius is only weakly correlated with the contrast ratio. As the permeability contrast increases from 5 to 50, the correlation between plume radius and contrast ratio becomes stronger. For example, in a reservoir where k_{high}/k_{low} = 50, the plume is 38% smaller than in a reservoir where k_{high}/k_{low} = 5. Once the contrast ratio is higher than 50, supercritical CO_2 travels only in the high permeability layers and the plume radius becomes independent of the contrast ratio. The plume is separated into multiple smaller plumes under each shale layer. In this case, the reservoir can be treated as separate flow

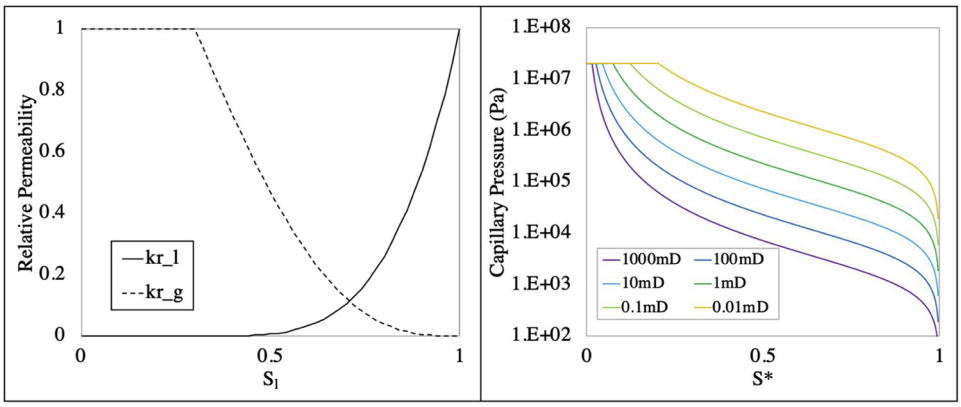

Fig. 2. (a) Relative permeability curve using the Corey's curves model, where S_{lr} = 0.3, S_{gr} = 0. (b) van Genuchten capillary pressure curves of representative materials, where $S^* = (S_l - S_{lr}) / (S_{ls} - S_{lr})$. Fitting parameter λ = 0.3, S_{lr} = 0.3, S_{ls} = 0.999, and P_{max} = 2.0E7 Pa.

units and the simulation can be performed within each unit if desired.

The percentage of the injected CO_2 that dissolves is another important model output. As shown in Fig. 3, CO_2 dissolves in water wherever supercritical CO_2 is present. The mass fraction of dissolved CO_2 is determined by the supercritical gas saturation, pressure, temperature, and salinity of the reservoir. To first order, the amount of CO_2 that dissolves is proportional to the volume of a supercritical CO_2 plume as shown in Fig. 7a. Here we define the volume of a supercritical CO_2 plume as the volume where CO_2 gas saturation is greater than 5% (see Fig. 7b). At a certain average gas saturation, a larger plume always causes larger CO_2 dissolution. At the same time, the gas saturation in a plume is inversely proportional to the volume, and also determines the total mass fraction of dissolved CO_2. A small amount (4–9%) of additional CO_2 dissolves at the leading edge of the plume when CO_2 first enters a grid cell and equilibrates with reservoir fluids. Note that the effect of dissolution-driven gravity current is not modeled in this paper due to the relatively short time frames. Diffusion can also contribute to dissolution, particularly for the highly heterogeneous reservoirs where a large surface area is between the plumes in the high permeability layers and adjacent low permeability layers. Therefore, the surface area

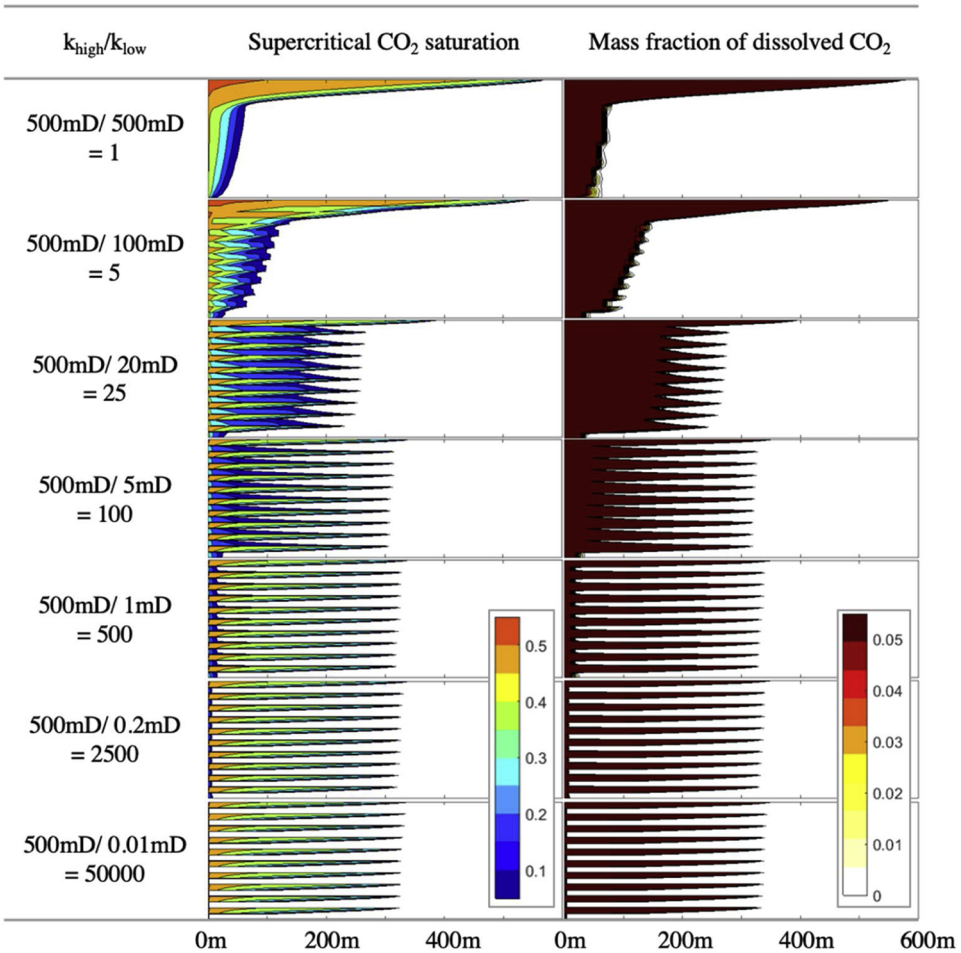

Fig. 3. Supercritical CO_2 saturation and mass fraction of dissolved CO_2 plots at representative contrast ratios. All results shown are evaluated at the end of the 3-year injection.

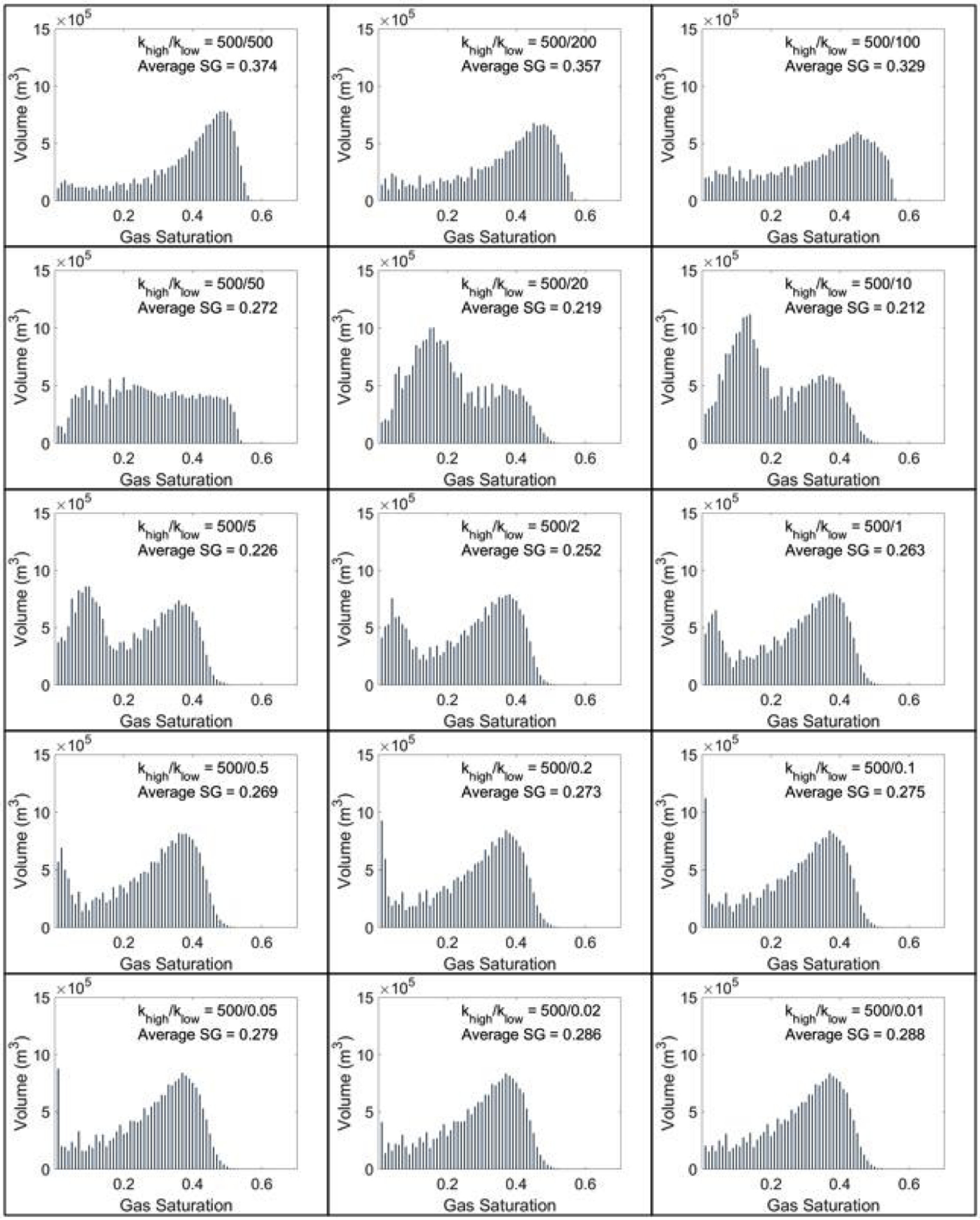

Fig. 4. Volume averaged histogram of supercritical CO_2 saturation for the base case simulations.

of a plume is another factor that contributes to the total amount of dissolution. Quantification of the extent of dissolution at the leading edge and surface area of the plume should be viewed with caution due to errors associated with numerical dispersion and volume averaging, particularly when grid cells are large. Convergence of the solutions for our grid (Appendix A) suggest that the errors are minimal, but values should still be viewed with caution.

Looking at the quantitative relationship between dissolution and the degree of permeability contrast (Fig. 6), we find that the amount of dissolution increases for contrast ratio up to 50. From the contrast ratio of 1 to 5, the dissolution gradually increases from 12% to 15% as the volume of the plume gradually grows larger. At the contrast ratio increases from 5 to 50, the extent of CO_2 dissolution becomes larger with up to nearly 22% of all of the CO_2 injected being dissolved. The maximum dissolution occurs at the contrast ratio of 50 with the lowest average gas saturation and highest plume volume. As the contrast ratio increases from 50 to 200, CO_2 dissolutions drops to about 17%. Lower dissolution percentages are explained by the lack of contact with the

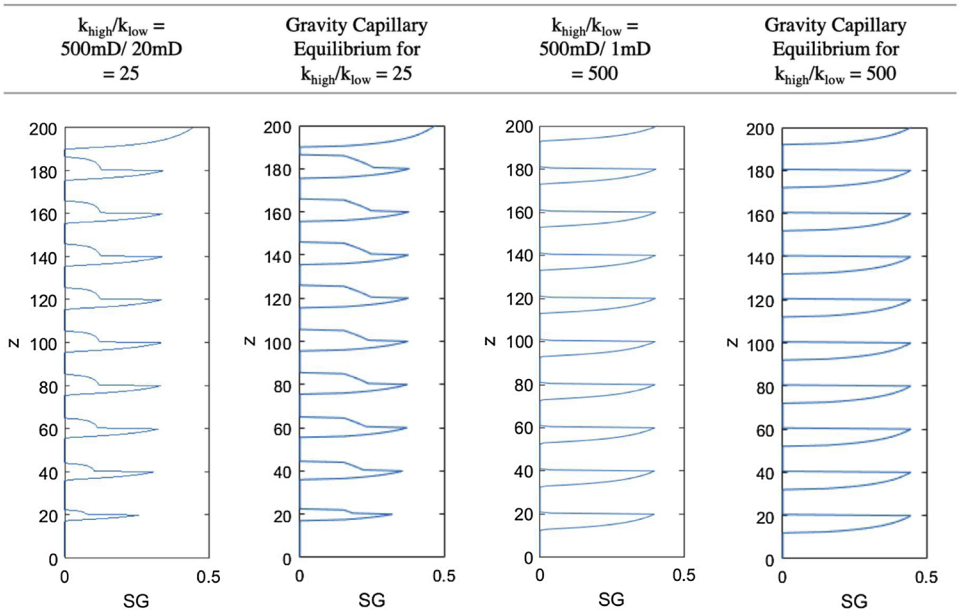

Fig. 5. Saturation profiles at 200 m away from the injection for reservoirs with permeability contrast of 25 and 500.

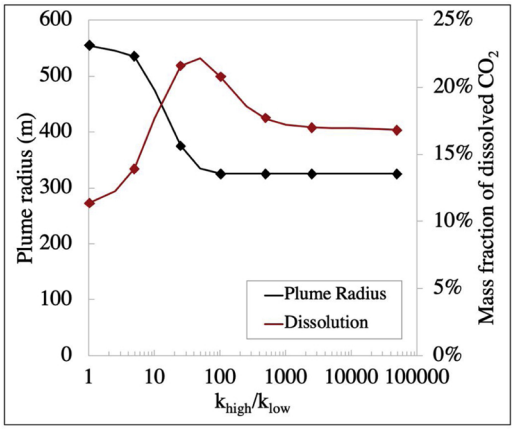

Fig. 6. Plume radius vs. permeability contrast and mass fraction of dissolved CO_2 vs. contrast ratio, each diamond shaped point corresponds to a representative contrast ratio that is displayed in Fig. 3.

water in the lower permeability layers and smaller plume volumes.

To investigate the sensitivity of our results to the reservoir permeability, we conduct similar analyses to reservoirs where the permeability of the higher permeability layers is 200 mD and 1000 mD (Fig. 8). It is important to note that we observe the same three regimes as identified in the 500 mD case. For lower permeability reservoirs, the ratio of viscous to gravitational forces is greater, thus counteracting the influence of gravity override that tends to increase the footprint of the plume. We also observe a similar trend in the relationship between dissolution and contrast ratio, where the maximum in the mass fraction of dissolved CO_2 occur at contrast ratios between 50 and 100. For the 1000 mD case, the maximum dissolution is the highest among the three cases. However, when the contrast ratio is lower than 50, the amount of dissolved CO_2 in the 1000 mD reservoirs are less than the other two cases because the plume quickly accumulates below the seal and forms a smaller plume with a higher average saturation.

Similarly, we extended the injection period to 10 years with a total of 3.65 Mtons of CO_2 and show the result in Fig. 9. We observe a very similar pattern of the three regimes for the relationship between the plume radius and the contrast ratio, except that the plume radius shrinkage due to increasing permeability contrast is even greater than for the base case (3 years of injection). When the contrast ratio is smaller than 100, the mass fraction of dissolved CO_2 in the 10 years case is less than the base case due to the larger CO_2 gravity tongues with higher gas saturation.

3.2. Modeling with Anisotropic permeability averages

Anisotropic permeability is commonly used in modeling to account for layered heterogeneity (Doughty and Pruess, 2004; Lengler et al.,

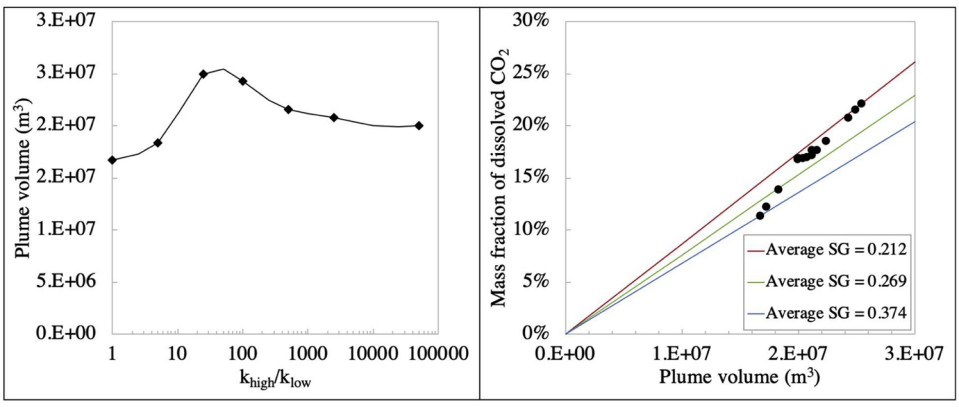

Fig. 7. (a) Plume volume (defined as greater than 5% gas saturation) vs. contrast ratio, each diamond shaped point corresponds to a plot of representative contrast ration displayed in Fig. 3. (b) Correlation between the mass fraction of dissolved CO_2 and the plume volume, each data point represents a simulation in the base case. The three lines show the relationship between the mass fraction of dissolved CO_2 and plume volume for three examples of fixed average gas saturation. The average gas saturations are correspond to contrast ratio of 25, 1000, and 1 respectively.

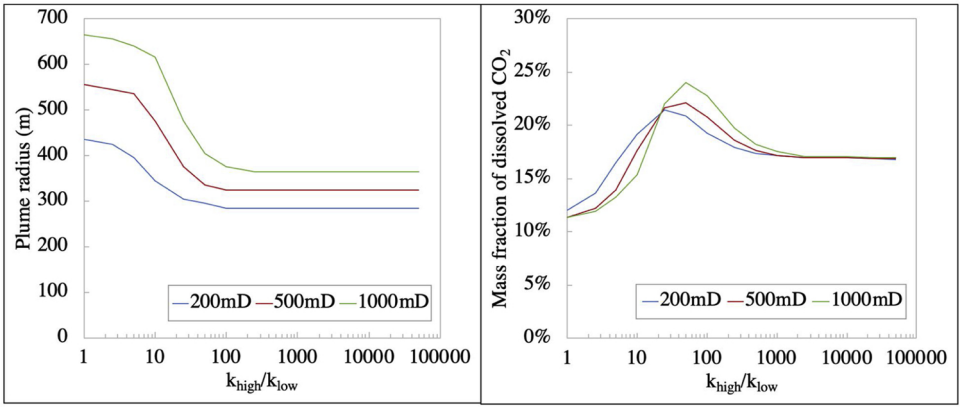

Fig. 8. (a) Comparison of plume radius vs. contrast ratio for the 200 mD case, base case (500mD), and 1000mD case. (b) Comparison of dissolution vs. heterogeneity for 200 mD case, base case (500mD) and 1000mD case.

2010; Strandli and Benson, 2013). However, it can be problematic to plume migration modeling by missing the influence of by thin heterogeneous layers. This phenomenon is known as the thief zone issue in oil and gas production as well as for CO_2-EOR reservoirs (Mcguire et al., 1998; Li et al., 2016). In this study, we develop a set of homogeneous anisotropic models to compare with models that explicitly account for heterogeneity. The effective horizontal and vertical permeability are calculated by the arithmetic and harmonic averages, respectively:

$$k_x = \frac{\sum_1^n k_j h_j}{\sum_1^n h_j} \tag{2a}$$

$$k_z = \frac{\sum_1^n h_j}{\sum_1^n h_j/k_j} \tag{2b}$$

The capillary pressure curve is constructed by the van Genuchten function where the capillary entry pressure is scaled by the Leverett-J function with the average permeability of k_x and k_z. The anisotropic models have the identical reservoir condition and grids as the heterogeneous models with a homogeneous anisotropic permeability assigned to each cell. The comparison of the supercritical CO_2 saturation are shown in Fig. 10 and summarized in Fig. 11.

Comparing the supercritical CO_2 plume radius results using the anisotropic model with the heterogeneous model Fig. 11a, we observe a small difference in plume radius (up to 11%) when the contrast ratio is smaller than 100 and anisotropy ratio is smaller than 26. As the contrast ratio increases, the anisotropic model underestimates the plume extent and the error increases with the contrast ratio as well as anisotropy ratio. At high contrast ratio, the corresponding anisotropy ratio becomes extremely high and the plume migration behaves as if there are no buoyancy forces, which results in a progressively more compact plume. Simulation results using an anisotropic permeability model can result in errors of up to 50% in plume radius at extremely high anisotropy (k_x/k_z = 12502).

The anisotropic permeability models also fail to simulate dissolution accurately as shown in Fig. 11b. For contrast ratios below 500 (anisotropy ratio below 126), the anisotropic models underestimate the amount of dissolution. The largest underestimation occurs at the contrast ratio of 25 and anisotropy ratio of 7, where the error by the anisotropic case is up to 25%. By employing anisotropic permeability to model heterogeneous reservoirs, the advantages of having more dissolution will be overlooked.

In Fig. 12, we compare the histograms of gas saturation distributions between the heterogeneous reservoirs and the corresponding anisotropic reservoirs at five representative contrast ratios. Unlike the bimodal distribution of gas saturation in the heterogeneous cases, a sole dominant gas saturation is found in the plume of anisotropic reservoirs. The average gas saturation gradually decreases as the anisotropy ratio increases. When the reservoir becomes extremely anisotropic (k_x/k_z = 6250.5), the reservoir behaves like a no-gravity system and numerical dispersion can be clearly observed at the leading edge of the plume.

Similar results are obtained for the 200 mD and 1000 mD reservoirs (Fig. 13a). For a contrast ratio less than 100 (anisotropy ratio less than 26), the 1000 mD anisotropic permeability case has errors in plume radius of up to 11% whereas the 200 mD anisotropic permeability case underestimates the plume radius by up to 19%. This indicates that, at low contrast ratio, using anisotropic permeability in lower permeability reservoirs results in more errors than in higher permeability reservoirs.

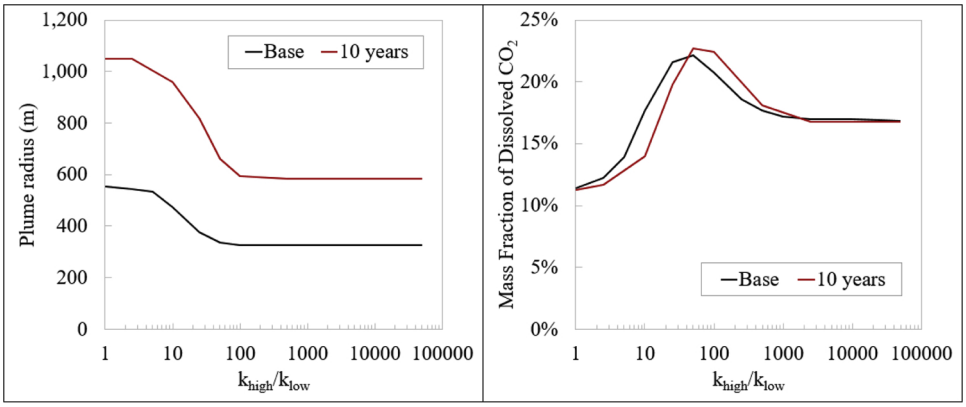

Fig. 9. (a)Plume radius and (b) mass fraction of dissolved CO_2 vs. contrast ratio where the injection time is extended to 10 years. The base case (3 years of injection) results in black are displayed for comparison.

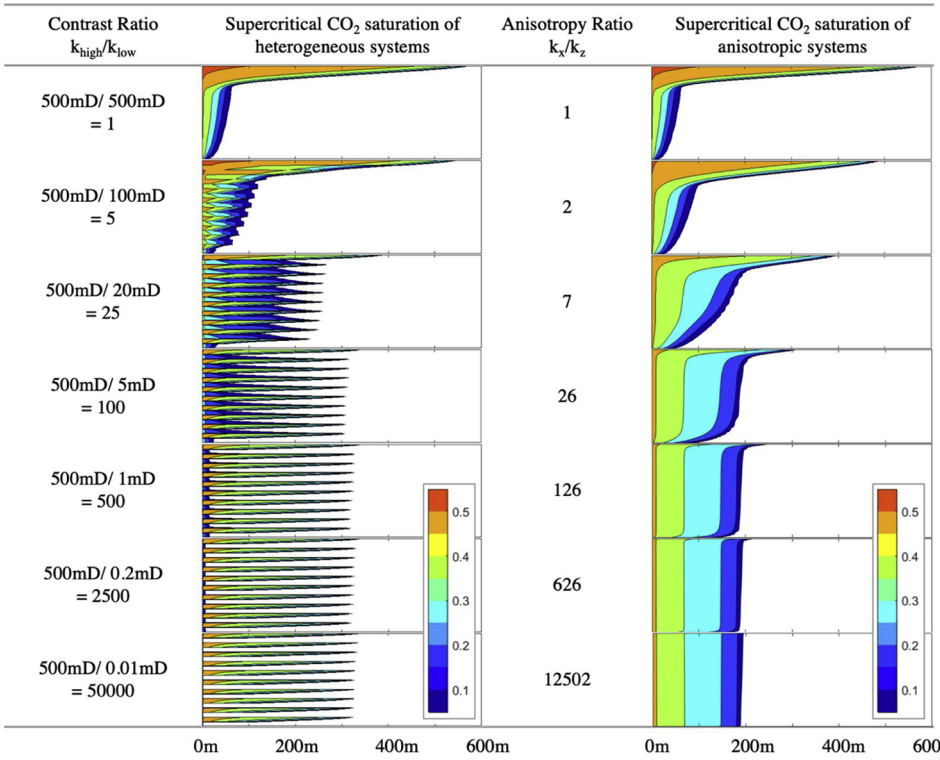

Fig. 10. Supercritical CO_2 saturation and mass fraction of CO_2 plot in heterogeneous and anisotropic reservoirs for the base (500 mD) case.

In contrast, at extremely high contrast ratio and anisotropy ratio, anisotropic models underestimate the plume radius by 47% for the 1000 mD case and 35% for the 200 mD case. This is due to the fact that a highly anisotropic reservoir always behaves like a no-gravity system while the actual plume radius in a heterogeneous reservoir depends on the permeability of the sandy layers.

For the relationship between the mass fraction of dissolved CO_2 and contrast ratio (Fig. 13b), very similar patterns are overserved for the 1000 mD and 200 mD cases, where the anisotropic model underestimates dissolution when the contrast ratio is less than 500 (anisotropy ratio less than 126). The maximum errors occur at higher contrast ratios and anisotropy ratios for higher permeability models.

3.3. Modeling with anisotropic relative permeability curves

In order to find a more accurate method to predict the plume radius and the mass fraction of dissolved CO_2 in layered systems with the anisotropic permeability, we attempted to use anisotropic relative permeability curves in addition to the anisotropic permeability averages k_x and k_z. The capillary pressure curve remains isotropic where the capillary entry pressure is scaled by the Leverett-J function with the average of k_x and k_z. To develop the anisotropic relative permeability curves, we assume capillary equilibrium between the high and low permeability layers. This allow us to calculate the saturation values in each layer and thus, the relative permeability in each layer. By analogy with calculating anisotropic permeability, anisotropic relative permeability curves can be calculated with the following equations (derivation is included in Appendix B):

$$k_{r,x} = \frac{k_{r,high}k_{high} + k_{r,low}k_{low}}{k_{high} + k_{low}} \tag{3a}$$

$$k_{r,z} = \frac{\frac{1}{k_{high}} + \frac{1}{k_{low}}}{\frac{1}{k_{high}k_{r,high}} + \frac{1}{k_{low}k_{r,low}}} \tag{3b}$$

Fig. 14a shows an example of the directional relative permeability curves calculated with the capillary equilibrium assumption where k_{high} = 500mD, k_{low} = 20mD. Red curves represent the horizontal flow

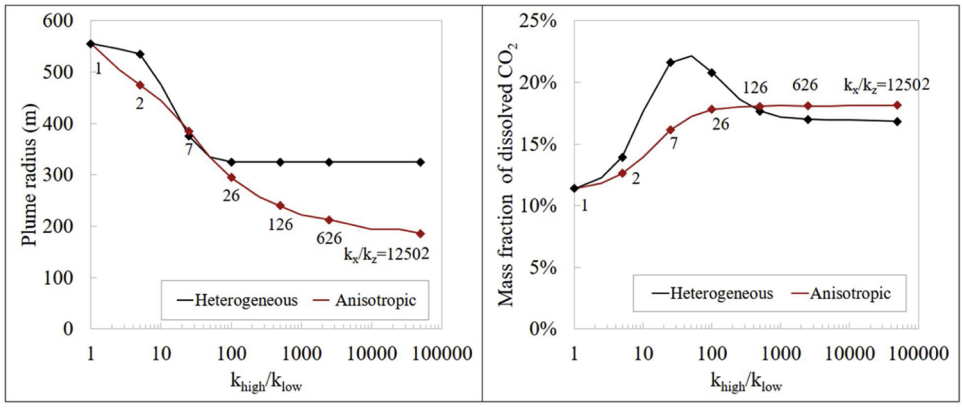

Fig. 11. (a) Comparison of plume radius vs. contrast ratio between heterogeneous and anisotropic systems, numbers on data points represents the anisotropy ratio for the representative cases displayed in Fig. 10. (b) Comparison of mass fraction of dissolved CO_2 vs. contrast ratio between heterogeneous and anisotropic systems, numbers on data points represents the anisotropy ratio for the representative cases displayed in Fig. 10.

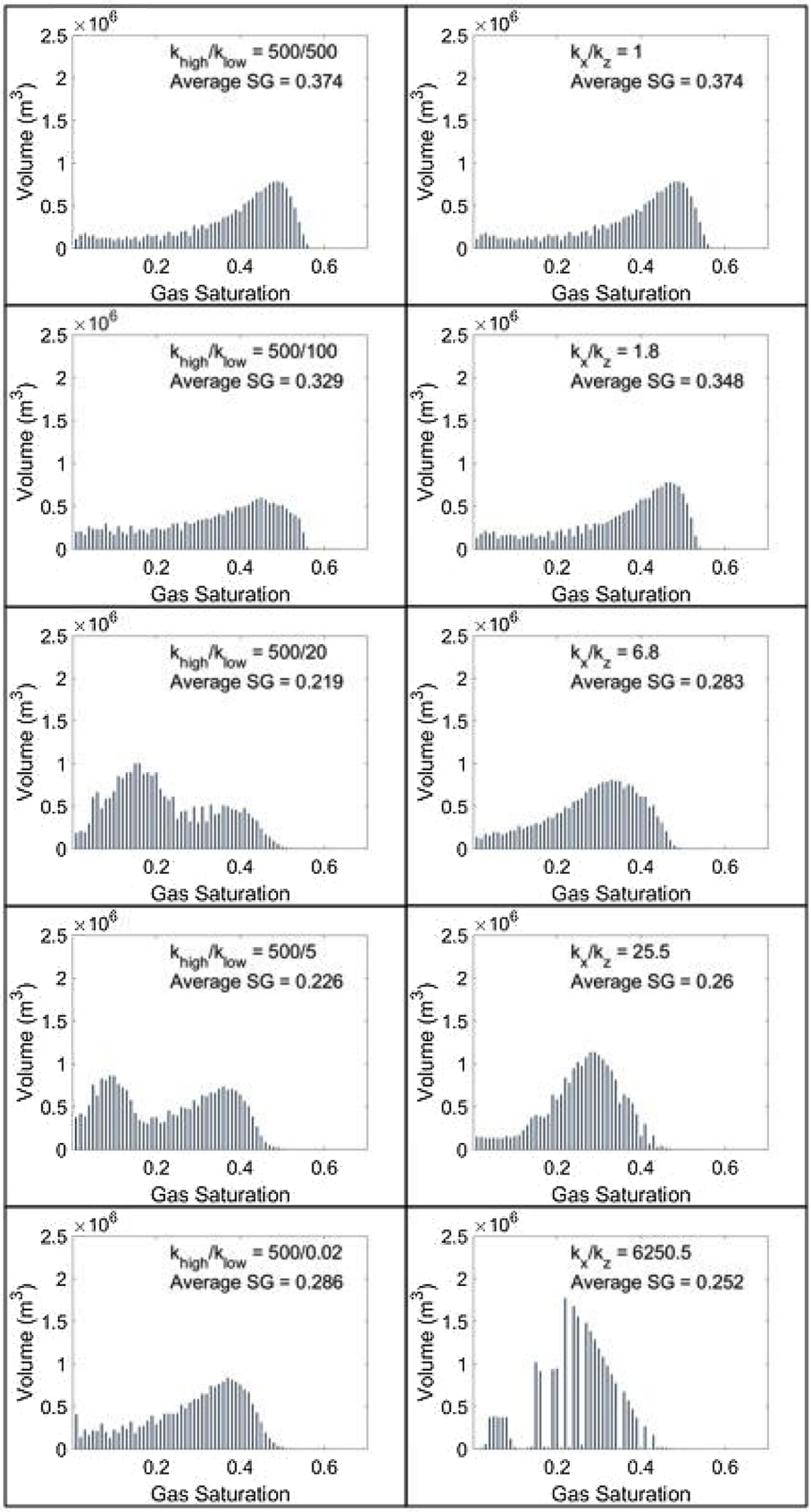

Fig. 12. Comparison of volume averaged histogram of supercritical CO_2 saturation between the heterogeneous and anisotropic models at representative contrast and anisotropy ratios.

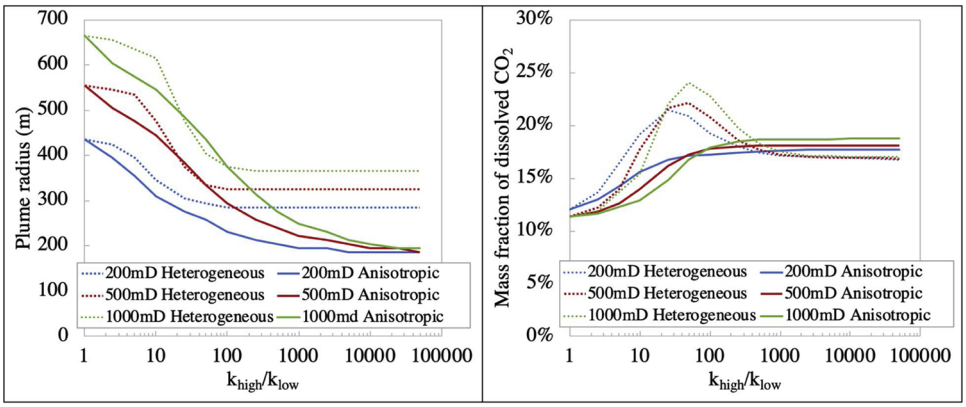

Fig. 13. (a) Comparison of plume radius vs. contrast ratio between heterogeneous and anisotropic systems in the base (500 mD), 200 md and 1000 mD cases. (b) Comparison of dissolution vs. contrast ratio between heterogeneous and anisotropic systems for the base (500 mD), 200 md and 1000 mD cases.

while blue curves represent the vertical flow. These directional relative permeability curves suggest that supercritical CO_2 is more mobile in the horizontal direction and less mobile in the vertical direction compared to the case for a homogenous setting. In contrast, liquid is more mobile in the vertical direction and less mobile in the horizontal direction. These analytical solutions agree with the measurements from previous studies (Corey and Rathjens, 1956; Iverson et al., 1996). Since TOUGH2 is unable to perform simulations with directional relative permeability curves, we utilized ECLIPSE300 to apply the directional relative permeability curves with the anisotropic permeability. ECLIPSE300 simulations were compared to the TOUGH2 and agreed well for the heterogeneous and permeability anisotropy cases. Results from simulations using both anisotropic permeability and anisotropic relative permeability are shown in Fig. 14b.

This result suggests that using directional relative permeability curves can only improve the agreement in plume radius between the anisotropic and heterogeneous models when the contrast ratio is lower than 10 (anisotropy ratio lower than 2). At higher contrast ratios, the directional anisotropic relative permeability promotes horizontal migration and causes overestimation of the plume radius. The largest error occurs at a contrast ratio of 50 and anisotropy ratio of 13, where the directional relative permeability model overestimates the plume radius by 42%. The occurrence of the three regimes in the relationship between the plume radius and contrast ratio is not captured by using the directional relative permeability either. Other approaches will be needed to accurately simulate plume migration in highly heterogeneous reservoirs.

4. Discussion

In Section 3.1, the simulations of plume migration in layered reservoirs show that the relationship between plume radius and the contrast ratio can be categorized into three distinct regimes. At moderate contrast ratio (1 to 5), CO_2 plumes are primarily governed by buoyancy and weakly correlated with contrast ratios. When the contrast ratio increases from 5 to 50, the majority of the plume is governed by gravity-capillary equilibrium and the plume radius decreases rapidly with increasing contrast ratio. When the contrast ratio is higher than 50, the vertical migration of CO_2 plume is prohibited, and the plume radius is no longer correlated with the contrast ratio. Similar results of the three regimes are observed in sensitivity studies for reservoir permeability, layer thicknesses, and injection time. The relationships between the mass fraction of CO_2 dissolution and contrast ratio are also analyzed for the layered heterogeneous systems. The maximum amount of dissolution often occurs at contrast ratio of 25 to 50.

In Section 3.2, we compared the plume radius and CO_2 dissolution results in the layered heterogeneous models with the models that uses anisotropic permeability averages. The comparison shows that the traditional anisotropic averages that are commonly utilized to capture layered heterogeneity do not do a good job in predicting plume radius when the contrast ratio is higher than 100 and the anisotropic ratio is higher than 26. The degree of anisotropy is commonly included in reservoir simulation models. The anisotropic permeability averages also fail to capture the behavior of CO_2 dissolution in heterogeneous reservoirs.

Sections 3.3 shows the results of using directional relative permeability curves with anisotropic permeability curves. Models using

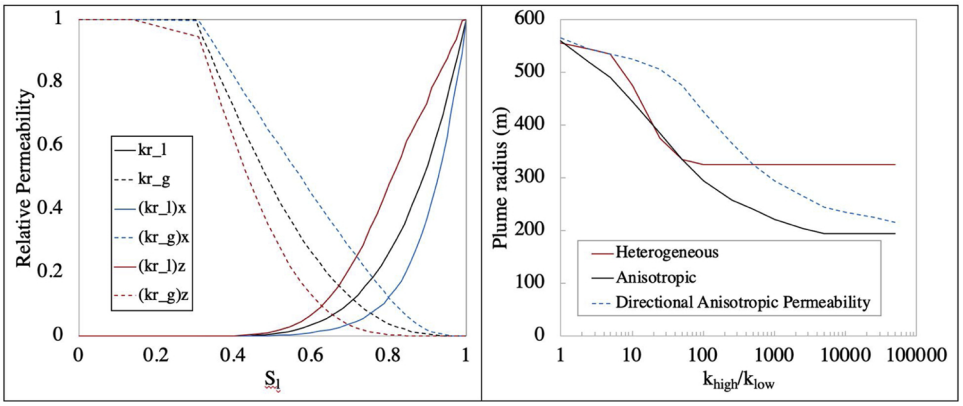

Fig. 14. (a) Directional relative permeability curves calculated for an example where k_{high} = 500mD and k_{low} = 20mD (b) Plume migration vs. contrast ratio result by using directional relative permeability in comparison with the heterogeneous and anisotropic base case.

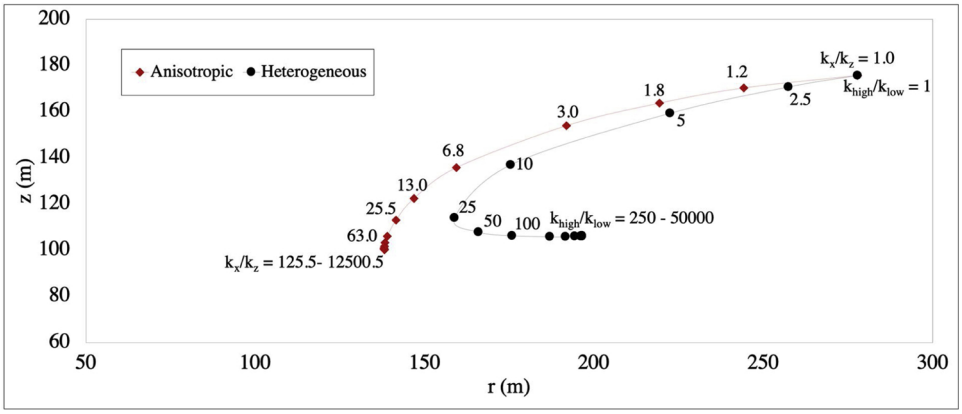

Fig. 15. Comparison of the mass weighted migration distance calculated for a cross section of plume between anisotropic and heterogeneous models. The labels represent contrast ratio and anisotropy ratio.

anisotropic relative permeability overestimate the plume radius for high contrast ratios and fail to capture the three regimens observed in heterogeneous reservoirs.

Taken together, this analysis suggests that accurate plume and dissolution modeling requires explicitly including details about the heterogeneous structure of the reservoir.

4.1. Mass weighted transport distance

The mass weighted transport distance is another way to characterize a plume, which describes the migration distance of the center of CO_2 plume mass away from the injection well. A plume mass that is closer to the injection well and the bottom of the reservoir generally has less risk of leakage and more efficient use of the pore space. In Fig. 15, each point represents the mass weighted migration distance in the vertical and radial direction. For example, the top right point represents the homogeneous case (k_{high}/k_{low} = 1), in which the whole plume mass travels farthest from the injection well and also closest to the seal. In the vertical direction, the mass weighted transport distance decreases as the contrast ratio increases and the whole plume mass is closer to the bottom of the reservoir. This is because the presence of heterogeneity restricts the vertical migration of CO_2. In the radial direction, the mass weighted transport distance has a non-monotonic relationship with the contrast ratio. When the contrast ratio is below 25, the mass weighted transport distance decreases rapidly as contrast ratio increases in the radial direction and the entire plume mass becomes closer to the injection well. At a contrast ratio of 25, the radial mass weighted transport distance is at its minimum, therefore has less risk of leakage and is beneficial for CO_2 storage. Once the contrast ratio is higher than 25, the migration distance of the whole plume mass again increases as contrast ratio gets bigger, but never to the extent it would in more homogeneous reservoirs. Furthermore, most of the plume is much deeper in the heterogeneous reservoir as compared to the homogeneous reservoir, which is again beneficial for CO_2 storage security.

Comparing the mass weighted migration distance in the heterogeneous models with the anisotropic models (Fig. 15), we find that the mass weighted migration estimated by all of the anisotropic models are closer to the injection well than the heterogeneous models. As the contrast ratio and anisotropy ratio increase, the differences of mass weighted migration distances on the radial direction becomes significant. At contrast ratio of 100 (anisotropy ratio of 63), the radial mass weighted migration distance in the anisotropic model is 200 m closer to the injection well compared to the heterogeneous model. Also, the anisotropic models fail to capture the non-monotonic relationship between the mass weighted migration distance in the radial direction and the contrast ratio.

4.2. Practical evaluation metrics

Sweep efficiency is an important parameter associated with CO_2 storage and enhanced oil recovery. In the context of this study where no oil is produced, we define the sweep efficiency as the fraction of reservoir pore volume contacted by separate gas phase CO_2. For the purpose of these calculations, the reservoir pore volume is defined as the porosity times the areal footprint of the plume times the total thickness of the reservoir. Fig. 16a summarizes the relationship between the sweep efficiency and the permeability contrast ratio for the 200 mD, 500 mD and 1000 mD cases. This figure indicates that high sweep efficiencies occur with high contrast ratios (greater than 100). Heterogeneous reservoirs in the 200 mD cases have the highest sweep

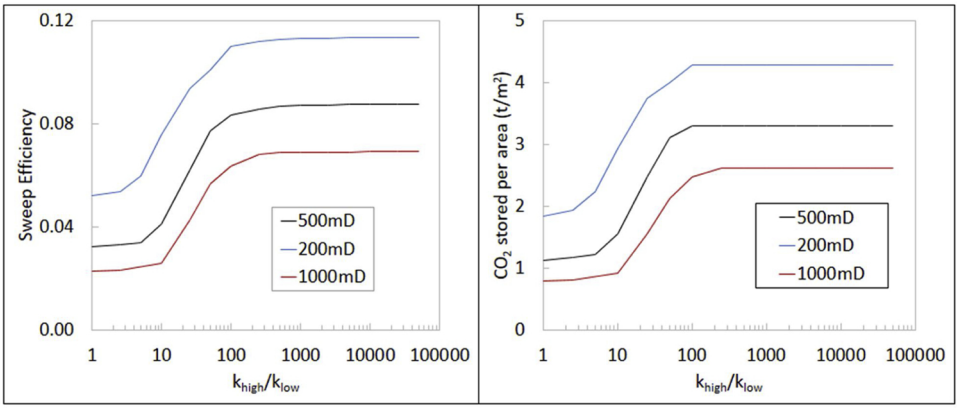

Fig. 16. (a) Sweep efficiency and (b) CO_2 stored per area for the cases studied here.

efficiencies (11%) because the mobility of the CO_2 is the lowest among all cases. In contrast, the sweep efficiencies for the 1000 mD cases range from 3 to 7%, showing that for both CO_2 storage and CO_2-EOR, the reservoir pore volume is used inefficiently.

Another evaluation metric that can be used in CO_2 site selection is the mass of CO_2 stored per unit area (t/m^2). For CO_2 storage sites, a reasonable range of the mass of CO_2 stored per unit area is about 0.5–5 t/m^2 (NAS, 2018). Our calculations fall within this range as shown in Fig. 16b. Heterogeneous reservoirs with a contrast ratio greater than 50 have more CO_2 stored per unit area. Also, lower permeability reservoirs have higher amounts of CO_2 storage per unit area.

5. Conclusions

In this study, we focus on modeling CO_2 storage in vertically layered heterogeneous reservoirs. By systematically investigating a wide range of permeability contrast ratios using high resolution numerical simulations, we quantify the relationship between plume radius, dissolution and permeability contrast ratio. The major conclusions are summarized as follows:

(1) The plume radius is highly sensitive to heterogeneity in the reservoir, varying by up to a factor of 2 for a range of realistic scenarios. The sensitivity of plume radius to contrast ratio falls into 3 distinct regimes: for contrast ratios smaller than 5, the plume radius is largest and nearly constant; as contrast ratio increases from 5 to 50, plume radii are highly sensitive to contrast ratio and decrease rapidly; at contrast ratios greater than 50 plume radius becomes nearly constant, but is about 40% smaller than for homogeneous reservoirs. This effect is explained by the role that low permeability (high capillary pressure) layers play in counteracting gravity forces that drive upward migration of the plume.
(2) Anisotropic permeability values can provide relatively accurate plume radius prediction for layered heterogeneity for contrast ratios of less than 100 (corresponding to permeability anisotropy of less than 26), where the errors are up to 11% in our base case. For higher contrast ratios, anisotropic models underestimate the plume radius by large amounts because they do not account of the fact that the capillary entry pressure of the low permeability layers prevents CO_2 from entering them.
(3) Dissolution of CO_2 during the injection phase also depends strongly on the permeability contrast ratio, reaching a maximum of nearly 25% at a contrast ratio of about 50. For homogeneous reservoirs or those with small permeability contrasts, dissolution is about 50% lower. For high contrast ratios, the amount of dissolution is between these two extremes. We show that dissolution correlates with plume volume, and the largest plume volumes correspond to permeability contrast ratios between 50 and 100.

This work has implications for both practical issues such as site selection and approaches for obtaining accurate information about plume migration. With regard to site selection, this work shows that moderate to high degrees of permeability heterogeneity (contrast ratios of up to 100) is advantageous insofar as it reduces the plume footprint, keeps the bulk of the plume deeper in the reservoir and away from the seal, and leads to higher dissolution rates. This work also demonstrates the need for high resolution simulations to model plume migration accurately. For modest levels of heterogeneity (< 25), anisotropic simulations can provide reliable estimates of plume radius, but for higher degrees of anisotropy, which are not unusual, alternative approaches are needed that capture the capillary behavior of heterogeneous systems. All of these simulations were carried out with purely vertically layered systems using radial geometry. In reality, the situation is more complex, but the insights gained here are relevant to the broader context of geological storage.

Acknowledgment

This work was supported by the Global Climate and Energy Project at Stanford University.

Appendix A. Grid selection

Since plume migration and the mass fraction of dissolved CO_2 are highly sensitive to cell thickness (Yamamoto and Doughty, 2011), we performed a sensitivity study with grid cell thicknesses of 10, 5, 2.5, 1 and 0.5 m cells. Representative plume CO_2 saturation plots using each grid are displayed in Fig. A17 for a range of values in k_{high}/k_{low}. Summary plots of plume radius (defined as $S_{CO2} = 0.05$) and CO_2 dissolution verses the contrast ratio are shown in Fig. A18.

As shown in Fig. A18a, the plume radius simulated with a grid thickness of "z = 0.5 m" converges with the "z = 1 m" case, which suggests that the accurate prediction of plume radius can be provided by the 1 m grid. When the reservoir is homogeneous (contrast ratio = 1), using the coarsest grid of "z = 10 m" generates approximately 9% error on the plume radius. This error in plume radius estimation increase to approximately 25% as the contrast ratio increases. The 10 m grid generates significant error at high contrast ratio because each high permeability layer is only represented by one cell. Having only 1 grid cell per layer prevents gravity override within each high permeability layer and consequently underestimates the plume radius. As a result, highly heterogeneous reservoirs are more vulnerable to plume radius errors than homogeneous reservoirs.

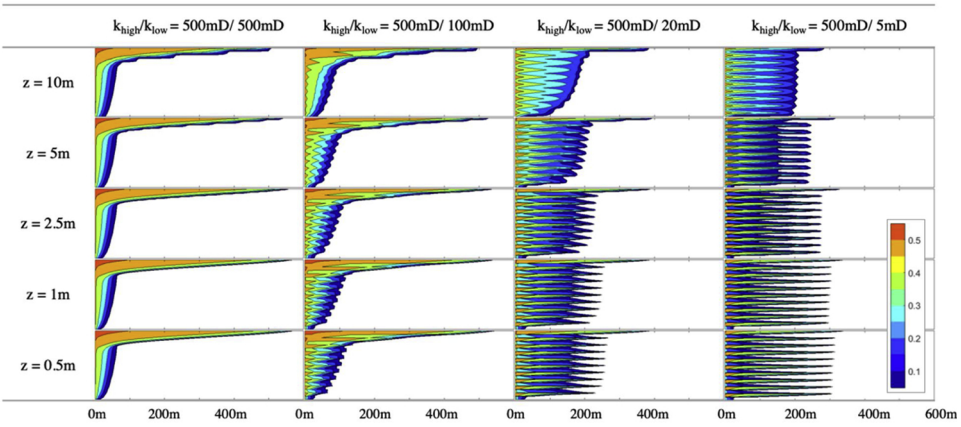

Fig. A17. Supercritical CO_2 saturation results comparison by using different cell thickness at different contrast ratios.

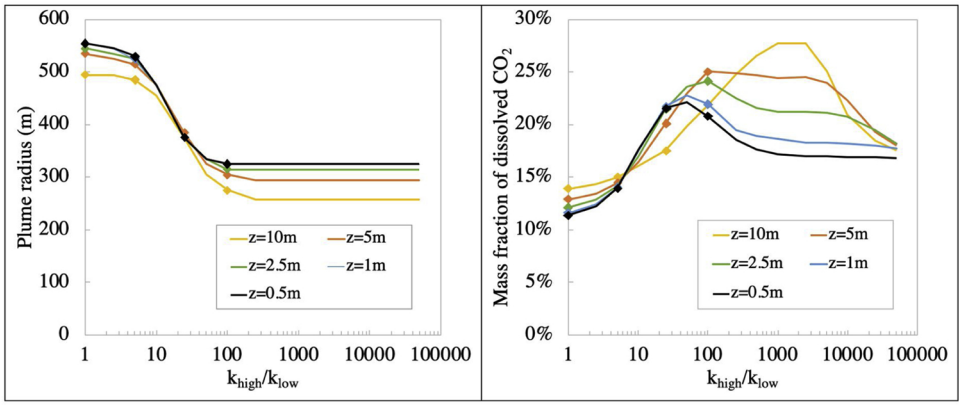

Fig. A18. (a) Plume radius vs. contrast ratio for each cell thickness. (b) Dissolution vs. heterogeneity for each cell thickness. Each point represents a plot in Fig. A18.

In addition to the plume radius, the choice of grid thickness also has a great impact on CO_2 dissolution as shown in Fig. A18b. The reasonably close agreement between results for the 1 m and 0.5 m-thick cells suggests that grid cell thickness of 0.5 m is adequate for these simulations.

Appendix B. Derivation of directional relative permeability equations

The absolute anisotropic permeability average for a layered system can be calculated as:

$$k_x = \frac{\sum_1^n k_j h_j}{\sum_1^n h_j} \tag{4a}$$

$$k_z = \frac{\sum_1^n h_j}{\sum_1^n h_j/k_j} \tag{4b}$$

Since the thicknesses of the higher and lower permeability layers are equal in our model, the anisotropic permeability averages can be simplified as:

$$k_x = \frac{10hk_{high} + 10hk_{low}}{10\ h + 10h} = \frac{k_{high} + k_{low}}{2} \tag{5a}$$

$$k_z = \frac{10\ h + 10h}{{}^{10h}/_{k_{high}} + {}^{10h}/_{k_{low}}} = \frac{2}{{}^{1}/_{k_{high}} + {}^{1}/_{k_{low}}} \tag{5b}$$

However, in the context of CCS, the effective permeability of supercritical CO_2 is calculated according to the relative permeability curves and the absolute permeability. Therefore, the anisotropic permeability average should be represented as:

$$k_{r,x}k_x = \frac{k_{r,high}k_{high} + k_{r,low}k_{low}}{2} \tag{6a}$$

$$k_{r,z}k_z = \frac{2}{{}^{1}/_{k_{high}k_{r,high}} + {}^{1}/_{k_{low}k_{r,low}}} \tag{6b}$$

By assuming capillary equilibrium over the volume that we are averaging, the relative permeability curves of the anisotropic permeability average are calculated as Eqs 3.

$$k_{r,x} = \frac{k_{r,high}k_{high} + k_{r,low}k_{low}}{k_{high} + k_{low}} \tag{3a}$$

$$k_{r,z} = \frac{\frac{1}{k_{high}} + \frac{1}{k_{low}}}{{}^{1}/_{k_{high}k_{r,high}} + {}^{1}/_{k_{low}k_{r,low}}} \tag{3b}$$

References

Bryant, S.L., Lakshminarasimhan, S., Pope, G.A., 2006. Buoyancy-dominated multiphase flow and its impact on geological sequestration of CO2. SPE/DOE Symp. Improv. Oil Recover. 22–26. https://doi.org/10.2118/99938-MS.

Cavanagh, A., Nazarian, B., 2014. A new and extended Sleipner Benchmark model for CO2 storage simulations in the Utsira Formation. Energy Procedia 63, 2831–2835. https://doi.org/10.1016/j.egypro.2014.11.305.

Corey, A.T., Rathjens, C.H., 1956. Effect of stratification on relative permeability. J. Pet. Technol. 8, 69–71. https://doi.org/10.2118/744-G.

Doughty, C., 2010. Investigation of CO2 plume behavior for a large-scale pilot test of geologic carbon storage in a saline formation. Transp Porous Med. https://doi.org/10.1007/s11242-009-9396-z.

Doughty, C., Pruess, K., 2004. Modeling supercritical carbon dioxide injection in heterogeneous porous media. Vadose Zone J. 3, 837–847. https://doi.org/10.2113/3.3.837.

EPA, 2013. Geologic Sequestration of Carbon Dioxide Underground Injection Control (UIC) Program Class VI Well Area of Review Evaluation and Corrective Action Guidance 96. https://doi.org/EPA816-R-13-001. .

Finley, R.J., 2014. An overview of the Illinois Basin – Decatur Project. Greenh. Gas Sci Technol 4, 571–579.

Flett, M., Gurton, R., Weir, G., 2007. Heterogeneous saline formations for carbon dioxide disposal: impact of varying heterogeneity on containment and trapping. J. Pet. Sci.

Eng. 57, 106–118. https://doi.org/10.1016/j.petrol.2006.08.016.
Frailey, S.M., 2013. Estimating CO2 plume size: a correlation for site screening. Int. J. Greenh. Gas Control 13, 230–234. https://doi.org/10.1016/j.ijggc.2012.11.033.
Gershenzon, N.I., Ritzi, R.W., Dominic, D.F., Mehnert, E., Okwen, R.T., Patterson, C., 2017. CO2trapping in reservoirs with fluvial architecture: sensitivity to heterogeneity in permeability and constitutive relationship parameters for different rock types. J. Pet. Sci. Eng. 155, 89–99. https://doi.org/10.1016/j.petrol.2016.09.008.
Han, W.S., Lee, S.-Y., Lu, C., McPherson, B.J., 2010. Effects of permeability on CO2 trapping mechanisms and buoyancy-driven CO2 migration in saline formations. Water Resour. Res. 46, 1–20. https://doi.org/10.1029/2009WR007850.
Hovorka, S.D., Doughty, C., Benson, S.M., Pruess, K., Knox, P.R., 2004. The impact of geological heterogeneity on CO2 storage in brine formations: a case study from the Texas Gulf Coast. Geol. Soc. London, Spec. Publ. 233, 147–163. https://doi.org/10.1144/GSL.SP.2004.233.01.10.
Ide, S.T., Jessen, K., Orr, F.M., 2007. Storage of CO2 in saline aquifers: effects of gravity, viscous, and capillary forces on amount and timing of trapping. Int. J. Greenh. Gas Control 1, 481–491. https://doi.org/10.1016/S1750-5836(07)00091-6.
Iverson, W.P., Dunn, T.L., Ajdari, I., 1996. Relative permeability anisotropy measurements in tensleep sandstones. 10Th SPE/DOE Symp. Impr. Oil Recover 2, 317–324. https://doi.org/10.2523/35435-MS. (Tulsa, 4/21-24/96) Proc.
Kumar, A., Ozah, R., Noh, M., Pope, G.A., Bryant, S., Sepehrnoori, K., Lake, L.W., 2005. Reservoir simulation of CO 2 storage in deep saline aquifers. 2004 SPE/DOE Symp. Improv. Oil Recover. pp. 17–21 Tulsa, 17–21 April.
Lengler, U., De Lucia, M., Kühn, M., 2010. The impact of heterogeneity on the distribution of CO2: numerical simulation of CO2storage at Ketzin. Int. J. Greenh. Gas Control 4, 1016–1025. https://doi.org/10.1016/j.ijggc.2010.07.004.
Li, D., Yang, J., Lu, D., 2016. Thief zone identification based on transient pressure analysis: a field case study. J. Pet. Explor. Prod. Technol. 6, 63–72. https://doi.org/10.1007/s13202-015-0168-8.
Mcguire, P.L., Fkdrnan, R.S., Group, T.S., 1998. Unconventional miscible EOR experience at Prudhoe Bay. Hydrocarb. Eng. 6, 10–18.
NAS, 2018. Negative Emissions Technologies and Reliable Sequestration, Negative Emissions Technologies and Reliable Sequestration. https://doi.org/10.17226/25259.
NETL, 2017. Best Practices : Risk Management and Simulation for Geologic Storage Projects 2017 Revised Edition.
Prats, M., Lake, L.W., 2008. The anisotropy of relative permeability. JPT Tech. Notes 60, 99.
Pruess, K., 2005. ECO2N: A Tough2 Fluid Property Module for Mixtures of Water, NaCl,and CO2. https://doi.org/10.2172/877331.
Pruess, K., Nordbotten, J., 2011. Numerical Simulation Studies of the Long-term Evolution of a CO 2 Plume in a Saline Aquifer with a Sloping Caprock. pp. 135–151. https://doi.org/10.1007/s11242-011-9729-6.
Pruess, K., Oldenburg, C., Moridis, G., 1999. TOUGH2 User's Guide. Rep. LBNL-43134 210.
Saeedi, A., 2012. Experimental Study of Multiphase Flow in Porous Media During CO2 Geo-sequestration Processes. https://doi.org/10.1007/978-3-642-25041-5.
Strandli, C.W., Benson, S.M., 2013. Diagnostics for reservoir structure and CO2 plume migration from multilevel pressure measurements. Energy Procedia 37, 4291–4301. https://doi.org/10.1016/j.egypro.2013.06.332.
Sung, R.T., Li, M.H., Dong, J.J., Lin, A.T.S., Hsu, S.K., Wang, C.Y., Yang, C.N., 2014. Numerical assessment of CO2 geological sequestration in sloping and layered heterogeneous formations: a case study from Taiwan. Int. J. Greenh. Gas Control 20, 168–179. https://doi.org/10.1016/j.ijggc.2013.11.003.
Yamamoto, H., Doughty, C., 2011. Investigation of gridding effects for numerical simulations of CO2 geologic sequestration. Int. J. Greenh. Gas Control 5, 975–985. https://doi.org/10.1016/j.ijggc.2011.02.007.
Zhang, Z., 2013. Numerical simulation and optimization of CO2 sequestration in saline aquifers. Comput. Fluids 80, 79–87. https://doi.org/10.1016/j.compfluid.2012.04.027.
Zweigel, P., Arts, R., Lothe, A.E., Lindeberg, E.B.G., 2004. Reservoir geology of the Utsira formation at the first industrial-scale underground CO2 storage site (Sleipner area, North Sea). In: Baines, S.J., Worden, R.H. (Eds.), Geological Storage of Carbon Dioxide. Geological Society of London.